Biomaterials Science

ROYAL SOCIETY OF CHEMISTRY

PAPER

View Article Online
View Journal | View Issue

Cite this: *Biomater. Sci.*, 2025, **13**, 2983

A hypoxia-activated and tumor microenvironment-remodeling nanoplatform for augmenting sonodynamic–chemodynamic-chemotherapy of breast cancer†

Chengxi Li,‡[a] Can Yang,‡[b] Tiantian Jiang,‡[a] Zheming Song,[a] Danling Cheng,[a] Jingchao Li, *[a] Yong Han*[c] and Ting Su*[a]

The tumor microenvironment (TME) offers a promising approach to enhancing cancer therapy by altering the conditions that support tumor growth and immune evasion. However, tumors are highly heterogeneous, and the TME can vary greatly even within different regions of the same tumor. Moreover, tumors can have evolving resistance mechanisms that limit the effectiveness of therapies. In this paper, we have designed a multifunctional nanoparticle named Lip-Ce6-MnO_2-TPZ, making sonodynamic therapy (SDT), chemodynamic therapy (CDT), and hypoxia-activated prodrugs work synergistically to maximize cancer treatment efficacy. The innovative Lip-Ce6-MnO_2-TPZ nanoparticle was constructed by loading Ce6, MnO_2, and hypoxia responsive drug tirapazamine (TPZ) together into a cytotoxic reactive oxygen species (ROS) responsive nanocarrier. Upon ultrasound (US) irradiation, ROS generated by Ce6 could not only induce cell apoptosis but also accelerate the disassembly of the nanoparticle for enhancing the release of TPZ and MnO_2. As a result, SDT consumed oxygen leading to the aggravation of the hypoxic condition in the tumor site for TPZ activation and DNA damage in tumor cells. Meanwhile, the MnO_2 was reduced to Mn^{2+} by GSH and caused antioxidant depletion. Mn^{2+} triggered CDT through a Fenton-like reaction by converting H_2O_2 to highly toxic •OH. Overall, the Lip-Ce6-MnO_2-TPZ platform could induce the generation of excess ROS combined with antioxidant depletion, resulting in oxidative stress and aberrant redox homeostasis of the TME. This strategy has brought forward the idea of inducing cancer cell death by synergistically working SDT, CDT, and hypoxia-activated prodrugs to maximize the therapeutic efficacy in cancer treatment.

Received 12th January 2025,
Accepted 7th April 2025

DOI: 10.1039/d5bm00060b

rsc.li/biomaterials-science

1. Introduction

Cancer remains one of the leading causes of death worldwide, with conventional therapies such as surgery, chemotherapy, and radiation often associated with significant side effects and limited efficacy, especially in advanced stages or resistant cancers. The tumor microenvironment representing a highly complex ecosystem of the solid tumor plays a critical role in tumor progression, survival, and therapy resistance.[1,2] This is attributed to the uncontrollable proliferation of cancer cells, which has high metabolic demands. As a result, a series of impacts are induced compared to normal tissues, such as the chaotic architecture of the tumor vasculature, acidic pH conditions, hypoxia, and aberrant redox homeostasis.[3–5] Tumor cells have evolved to tolerate and thrive under this stressful environment. They can even accelerate malignancy leading to drug resistance and treatment failure.[6,7] In recent years, there has been an increasing focus on developing therapies that specifically target the TME, either by modifying the microenvironment to make it more conducive to therapy or by directly attacking the stromal and immune cells that support tumor growth.[8,9]

Sonosensitizer-assisted sonodynamic therapy (SDT) in cancer therapy is highlighted by using low-intensity ultrasound (US) to activate the crucial sonosensitizers generating cytotoxic reactive oxygen species (ROS) to induce tumor cell apoptosis.[10] Ultrasound could target tumors in deep tissues

[a]*State Key Laboratory of Advanced Fiber Materials, College of Biological Science and Medical Engineering, Donghua University, Shanghai 201620, China. E-mail: jcli@dhu.edu.cn, suting@dhu.edu.cn*
[b]*Department of Obstetrics and Gynecology, The First Affiliated Hospital of Chongqing Medical and pharmaceutical College, Chongqing 400060, China*
[c]*State Key Laboratory of Oncogenes and Related Genes, Department of Oncology, Shanghai General Hospital, School of Medicine, Shanghai Jiao Tong University, Shanghai 200080, China. E-mail: hanrong2002@163.com*

†Electronic supplementary information (ESI) available. See DOI: https://doi.org/10.1039/d5bm00060b

‡These authors equally contributed to this work.

effectively due to deeper tissue penetration when compared with photodynamic therapy (PDT).[11,12] It is a promising strategy for tumor treatment owing to the therapeutic advantages of its non-invasive therapeutic modality, high controllability, and low toxic side effects. Despite the encouraging advantages of SDT in the applicability for cancer therapy, single SDT treatment makes it difficult to completely eradicate tumors and inhibit tumor recurrence due to the extremely complex and diverse tumor microenvironment.[13] Hypoxia is a common condition in a wide variety of solid tumors due to aberrant cancer cell proliferation and distorted blood vessels in the tumor site.[14] During SDT, sonosensitizers react with oxygen to generate cytotoxic ROS, which will consume oxygen and further aggravate the hypoxic condition in the tumor site.[15] This subsequently reduces the oxygen levels and limits the SDT efficiency contrarily. On the other hand, glutathione (GSH) with high antioxidant activity owing to high metabolic rates is critical for dampening ROS levels, presenting a major limitation for the SDT results as well.[16,17] Thus, other therapeutic modalities become progressively decisive to be combined to avoid the limitation of SDT.[18,19]

Chemodynamic therapy (CDT) is a novel tumor treatment strategy based on the reaction between catalysts and hydrogen peroxide (H_2O_2), which is inherently in excess in the tumor microenvironment compared to that in normal tissues.[20,21] As a result, the generation of highly toxic hydroxyl radicals (•OH) *via* a Fenton or Fenton-like reaction could efficiently kill cancer cells.[22,23] Unlike traditional treatment methods, CDT induced cell death through endogenous chemical reactions within the cells, which has been used for the treatment of different types of tumors.[24] Moreover, CDT can remodel the tumor immunosuppressive microenvironment by inducing immunogenic cell death (ICD) and improving the therapeutic efficiency of SDT.[25,26] Recently, besides iron, a variety of other transition-metal ions, such as Mn^{2+}, Cu^{2+}, Ni^{2+} and Co^{2+}, have been applied rigorously to fabricate nanoplatforms for cancer treatment *via* CDT.[27–29] Despite promising results in cancer treatment, CDT faces several challenges that limit its effectiveness and clinical application. The agents used for CDT often face poor penetration into dense tumor tissue, and the off-target effects, which can lead to systemic toxicity and oxidative damage in healthy tissues.[30,31] More importantly, the hypoxic

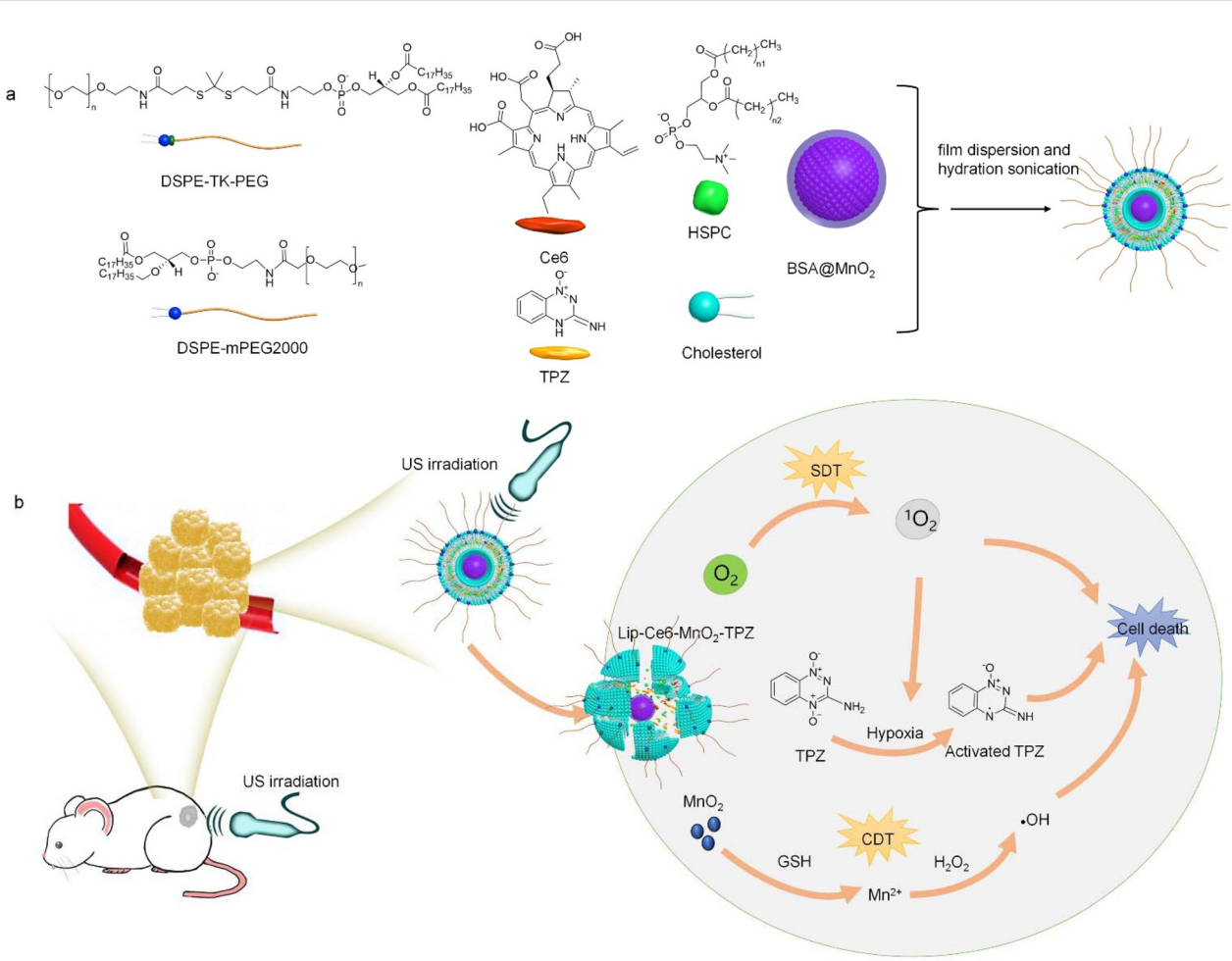

Fig. 1 Design of Lip-Ce6-MnO_2-TPZ that can combine chemokinetic and sonodynamic therapy for the treatment of breast cancer: (a) synthesis method of Lip-Ce6-MnO_2-TPZ and (b) schematic illustration of US-activatable Lip-Ce6-MnO_2-TPZ for the treatment of breast cancer.

environment can impede CDT since oxygen is necessary for ROS amplification, which decreases the therapeutic efficacy of CDT.[32] Developing nanoparticle delivery systems that can target the tumor site may enhance the penetration ability of the CDT agents.[33]

In recent years, nanotechnology has emerged as a promising tool for enhancing drug delivery, improving the pharmacokinetics of therapeutic agents, and enabling combination therapies that can target multiple aspects of the tumor. Despite these advances, the complexity of cancer and the heterogeneity of tumors continue to present significant challenges in developing universally effective treatments. To address the abovementioned challenges, our study endeavors to design and synthesize a ROS-responsive nanoplatform.[34] Innovative Lip-Ce6-MnO_2-TPZ was fabricated by a film hydration method, which encapsulated the sonosensitizer Ce6, MnO_2 for CDT, and hypoxia responsive drug tirapazamine (TPZ) together.[35,36] This ROS-responsive nanoplatform successfully delineates the synergizing effects of SDT and CDT for cancer treatment.[37] As depicted in Fig. 1, when the nanoparticle circulated through the bloodstream and accumulated in the tumor site, Ce6 generated ROS under US stimuli for cancer cell apoptosis.[38] ROS induced the breakage of the TK bond and accelerated the disassembly of the nanoparticle to enhance the release of TPZ and MnO_2.[39] Besides, SDT consumed oxygen and aggravated the hypoxic condition in the tumor site, leading to the activation of TPZ.[40,41] Activated TPZ further enhances oxidative damage, leading to DNA damage and tumor cell death. Meanwhile, the MnO_2 was reduced to Mn^{2+} and caused GSH depletion. Subsequently, Mn^{2+} triggered CDT through a Fenton-like reaction by converting H_2O_2 to highly toxic •OH.[42,43] As a result, the generation of excess ROS and antioxidant depletion combined together in the tumor cells caused aberrant redox homeostasis and modulation of the tumor microenvironment. Taking together, the Lip-Ce6-MnO_2-TPZ platform induces cancer cell death by making SDT, CDT, and hypoxia-activated prodrugs work synergistically to maximize the therapeutic efficacy in cancer treatment.

2. Materials and methods

2.1. Materials

Chlorin e6 was provided by Aladdin (China). TPZ was purchased from Selleckchem (USA). Bovine serum albumin (BSA) and $KMnO_4$ were obtained from Aldrich (Shanghai, China). 20,70-Dichlorodihydrofluorescein diacetate (H2DCFDA) and 1,2-distearoyl-*sn-glycero*-3-phosphoethanolamine-*N*-[methoxy (polyethylene glycol)] (DSPE-mPEG) were purchased from Shanghai Macklin Biochemical Technology Co., Ltd (China). A singlet oxygen sensor green (SOSG) and Cell counting kit-8 (CCK-8) were obtained from Molecular Probes Inc. (USA).

2.2. Characterization

The morphological characteristics were evaluated using a Tecnai G2 transmission electron microscope (TEM). The UV and fluorescence properties of nanoparticles were detected using an ultraviolet spectrophotometer (Persee, TU-1810, Beijing, China) and a fluorescence spectrophotometer (SHIMADZU, RF-6000, Kyoto, Japan), respectively. The sizes and zeta potential of nanoparticles in aqueous solutions (10 μg mL^{-1}) were evaluated using a Malvern Zetasizer Nano S90 analyzer.

2.3. Synthesis of Lip-Ce6-MnO_2

DSPE-mPEG (15 mg), DSPE-TK-PEG (5 mg), HSPC (20 mg) and cholesterol (5 mg) were dissolved in 5 mL chloroform, and Ce6 (1 mg) was dissolved in 1 mL tetrahydrofuran, respectively. Then the two solutions were mixed and the solvent was evaporated in a 40 °C water bath to obtain a thin film. BSA (16.7 mg) and $KMnO_4$ (2.1 mg) were dissolved in 3 mL water and stirred for 2 h. Then, the solution was added to a flask to dissolve the thin film and hydrated at 60 °C for 1 h with stirring. The obtained solution was sonicated for 1 h in an ice bath. To obtain the Lip-Ce6-MnO_2 nanoagent, the product was purified *via* ultrafiltration under centrifugation (2000 rpm, 1 h).

2.4. Synthesis of Lip-Ce6-MnO_2-TPZ

DSPE-mPEG (15 mg), DSPE-TK-PEG (5 mg), HSPC (20 mg), cholesterol (5 mg), and TPZ (0.5 mg) were dissolved in 5 mL chloroform and Ce6 (1 mg) was dissolved in 1 mL tetrahydrofuran. The two solutions were added into one flask and the solvent was removed using a 40 °C water bath. BSA (16.7 mg) and $KMnO_4$ (2.1 mg) were dissolved in 3 mL water and stirred for 2 h. Then, the thin film was dissolved in the obtained solution and hydrated at 60 °C under stirring for 1 h. The obtained solution was sonicated for 1 h in an ice bath. The resulting solution was purified *via* ultrafiltration under centrifugation (2000 rpm, 1 h) to obtain the final nanoagent.

2.5. Evaluation of the stability

Lip-Ce6-MnO_2 and Lip-Ce6-MnO_2-TPZ were dispersed in aqueous solutions at a final concentration of 10 μg mL^{-1} and stored at −4 °C. The hydrodynamic diameters of the samples were measured by DLS at 0, 7, and 14 days, respectively, to evaluate the stability.

2.6. Evaluation of $^1O_2$ generation

SOSG was a probe used to detect the generation of $^1O_2$. Lip-Ce6-MnO_2 or Lip-Ce6-MnO_2-TPZ was diluted to a concentration of 10 μg mL^{-1} and SOSG (3 μL, 500 μM) was added to the solution. The fluorescence intensities of the solution were measured after 0, 2, 4, 6, 8 and 10 minutes of US (1.0 W cm^{-2}). The efficiency of $^1O_2$ generation was demonstrated by the multiple of fluorescence intensity increase.

2.7. Evaluation of Fenton-like reaction

MB was a •OH indicator used for detecting the generation of •OH *via* Fenton-like reaction. Lip-Ce6-MnO_2, Lip-Ce6-MnO_2-TPZ, GSH (final concentration = 1 mM) and MB were added to an aqueous solution of $NaHCO_3$ with US for 10 min. After incubation for 30 min, MnO_2 in Lip-Ce6-MnO_2 and Lip-Ce6-

MnO_2-TPZ was reduced to Mn^{2+}, and then H_2O_2 (final concentration = 100 μM) was added to induce a Fenton-like reaction with Mn^{2+} to produce •OH. The absorption of MB solution was measured at 650 nm to evaluate the production of •OH.

2.8. Assessment of the drug release property

Lip-Ce6-MnO_2-TPZ was dispersed in aqueous solution at a concentration of 100 μg mL^{-1}. The solution was sonicated using ultrasonic treatment (1.0 W cm^{-2}) for 0 min, 5 min, 10 min and 15 min, respectively. The release efficiency of TPZ was evaluated using HPLC.

2.9. *In vitro* cytotoxicity evaluation

4T1 cancer cells were incubated with PBS, H_2O_2 (final concentration = 100 μM), Lip-Ce6-MnO_2 and Lip-Ce6-MnO_2-TPZ (Ce6 concentration = 0, 3.125, 6.25, 12.5, 25 and 50 μg mL^{-1}), under hypoxic conditions for 12 h. After incubation, the cells were washed with PBS and cultured in a medium containing CCK-8. Then, the cell viability was determined by CCK-8 analysis.

2.10. Evaluation of therapeutic effects *in vitro*

4T1 cancer cells were incubated with H_2O_2 (final concentration = 100 μM), Lip-Ce6-MnO_2 and Lip-Ce6-MnO_2-TPZ (Ce6 concentration = 10 μg mL^{-1}) under normoxic and hypoxic conditions for 12 h and the cells were subjected to US treatment (1.0 W cm^{-2}) for 3 min. After the cells were cultured for 12 h under normoxic and hypoxic conditions, the cell viability was measured by CCK-8 analysis.

2.11. *In vitro* cellular uptake evaluation

4T1 cells were incubated with Lip-Ce6-MnO_2 and Lip-Ce6-MnO_2-TPZ (Ce6 concentration = 10 μg mL^{-1}) for 12 h. The cells were washed with PBS and collected. On the one hand, the uptake of Lip-Ce6-MnO_2 and Lip-Ce6-MnO_2-TPZ by cells was assessed by flow cytometry (Beckman Coulter, Full Coulter, Fullerton, CA, USA), and on the other hand, cellular uptake assessment of the collected cells was performed using confocal fluorescence microscopy. Fluorescence intensity measurements were performed with ImageJ software.

2.12. Assessment of the intracellular GSH level

4T1 cells were incubated with Lip-Ce6-MnO_2 and Lip-Ce6-MnO_2-TPZ for 12 h and then the cells were subjected to US treatment (1.0 W cm^{-2}, 3 min). After culture for another 12 h, the cells were collected to measure the GSH level using a GSH/GSSG assay kit.

2.13. Evaluation of intracellular ROS production

H2DCFDA was a fluorescent probe used to detect the generation of intracellular ROS. 4T1 cells were incubated with Lip-Ce6-MnO_2 and Lip-Ce6-MnO_2-TPZ for 24 h. Then the cells were cultured in medium containing H2DCFDA for 30 min. After incubation, 4T1 cells were subjected to US treatment (1.0 W cm^{-2}) for 3 min. An inverted fluorescence microscope was used to detect fluorescence signals and evaluate intracellular ROS production.

2.14. Establishment of subcutaneous tumor models

All animal procedures were performed in accordance with the Guidelines for Care and Use of Laboratory Animals of Donghua University and approved by the Animal Ethics Committee of Donghua University. 4T1 cells were injected subcutaneously into each BALB/c mouse to build a mouse model of subcutaneous breast cancer.

2.15. *In vivo* fluorescence imaging and biodistribution analysis

The 4T1 cancer mouse models were injected with Lip-Ce6-MnO_2 and Lip-Ce6-MnO_2-TPZ (300 μg mL^{-1}, 200 μL) *via* the tail vein. To study nanoparticle accumulation into orthotopic pancreatic tumors, an IVIS fluorescence imaging system was used to image the mice (excitation: 640 nm, emission: 700 nm) at 0, 4, 8, 12, 24, 30 and 36 h. The fluorescence intensity of the tumor sites was quantified using Living Image software. After 36 h of injection, 4T1 tumor-bearing mice were sacrificed and major organs and tumors were taken for fluorescence imaging. The fluorescence intensity of major organs and tumors was quantified using Living Image software.

2.16. *In vivo* clearance study

After tail intravenous injection of Lip-Ce6-MnO_2 and Lip-Ce6-MnO_2-TPZ (300 μg mL^{-1}, 200 μL), living mice and the collected feces were imaged with the IVIS imaging system at different days post-injection. In addition, after 24 days of systemic administration, the mice were euthanised and the main organs were taken to detect their fluorescence signals.

2.17. *In vivo* therapeutic efficacy evaluation

The mice with 4T1 tumor-bearing cancer were i.v. injected with PBS, Lip-Ce6-MnO_2 and Lip-Ce6-MnO_2-TPZ (300 μg mL^{-1}, 200 μL). After 24 h, the 4T1 cancer cells were subjected to US treatment (10 min). The volume of the tumors was monitored every 2 days, and the weight of the mice was recorded, and after 18 days, the mice were sacrificed, and the tumors were photographed and weighed. Tumors and major organs were taken for hematoxylin and eosin H&E staining.

2.18. *In vivo* detection of intratumoral ROS production

4T1 tumor mouse models were injected with PBS, Lip-Ce6-MnO_2 and Lip-Ce6-MnO_2-TPZ (200 μL, 300 μg mL^{-1}). After 24 h, 25 μL of H2DCFDA in PBS solution (150 μM) was injected into the tumors. After 2 h, the tumors were subjected to US treatment (1.0 W cm^{-2}) for 10 min. Two hours after US treatment, the tumors were collected and used for ROS level evaluation using fluorescence imaging.

2.19. Statistical analysis

The data were reported as mean ± SD and the sample numbers (n) were provided. The significant differences were indicated by using One-way ANOVA analysis ($^*p < 0.05$, $^{**}p < 0.01$, and $^{***}p < 0.001$).

3. Results and discussion

3.1 Fabrication and characterization of the nanoparticles

The morphology and size distribution of these two nanoparticles were evaluated by TEM and DLS.[44] As shown by TEM images (Fig. 2a), they had homogeneous spherical shapes around 50 nm. The hydrodynamic diameters of Lip-Ce6-MnO_2 and Lip-Ce6-MnO_2-TPZ were 22.72 nm and 27.26 nm with zeta potentials of −23.1 mV and −19.8 mV, respectively, as measured by DLS (Fig. 2b and c). After fourteen days of storage, the hydrodynamic diameters of Lip-Ce6-MnO_2 and Lip-Ce6-MnO_2-TPZ remained almost unchanged, which showed their good stability (Fig. S1†). UV-Vis and fluorescence measurements were used to demonstrate the optical properties. Both Lip-Ce6-MnO_2 and Lip-Ce6-MnO_2-TPZ showed an absorption peak at 670 nm from Ce6. Moreover, Lip-Ce6-MnO_2-TPZ possessed a characteristic absorption peak of TPZ at 270 nm, indicating the successful loading of TPZ (Fig. 2d). In the fluorescence spectrum, both nanoparticles exhibited typical fluorescence emissions of Ce6 at 600–750 nm (Fig. 2e). The encapsulation efficiency and loading capacity were evaluated by HPLC for TPZ and UV-Vis spectroscopy for Ce6. As calculated, the encapsulation efficiency of TPZ and Ce6 was 84.58% and 81.47%, respectively, and the loading capacity was 0.65% and 1.25%, respectively. The singlet oxygen ($^1O_2$) generation under sonodynamic treatment was evaluated using singlet oxygen sensor green (SOSG) as the fluorescence probe. After irradiation, fluorescence intensity relative to 0 min at

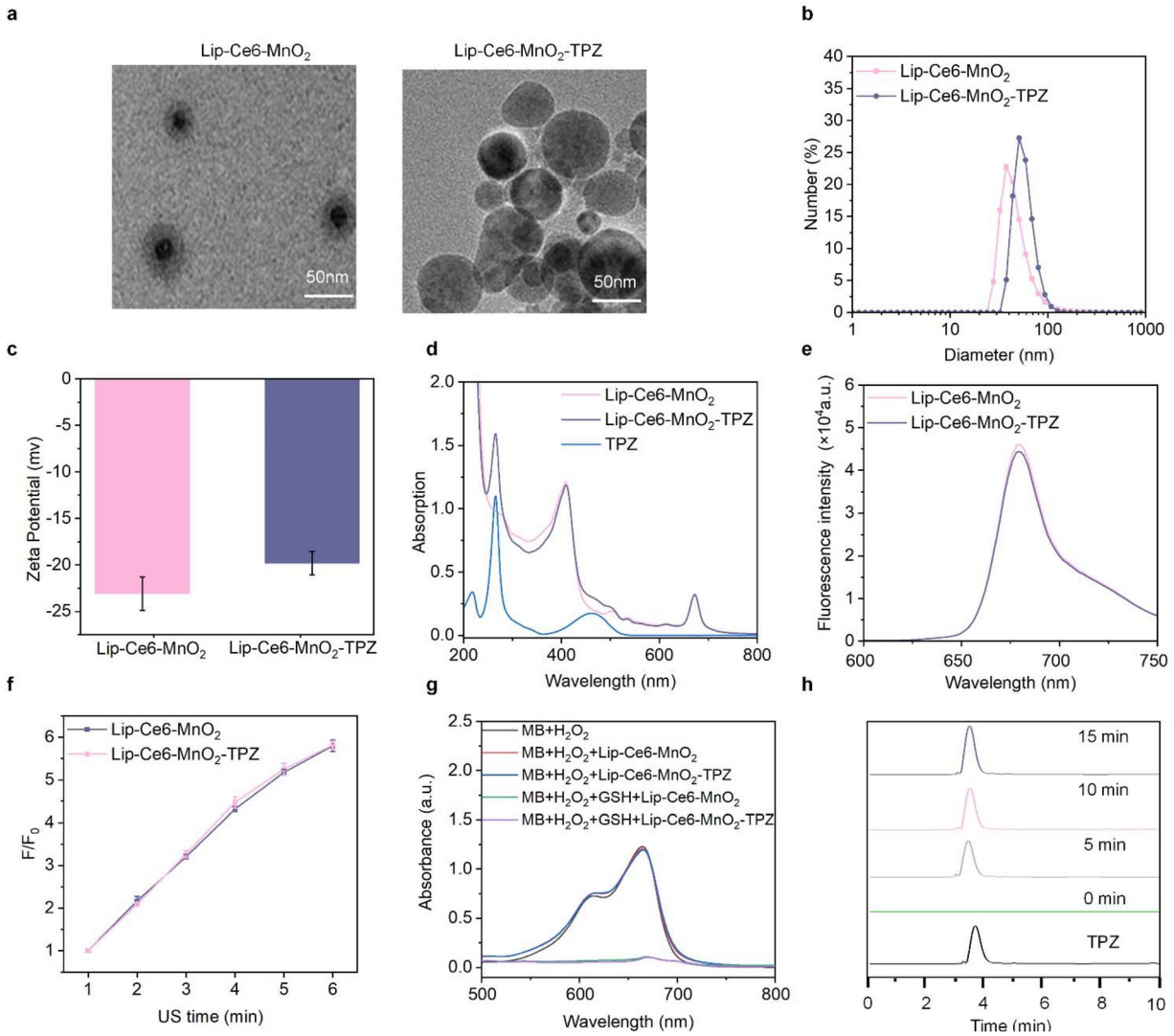

Fig. 2 Characterization of nanoparticles: (a) morphological characterization of Lip-Ce6-MnO_2 and Lip-Ce6-MnO_2-TPZ by TEM. (b) Particle diameter size of Lip-Ce6-MnO_2 and Lip-Ce6-MnO_2-TPZ; (c) measurements of the zeta potentials of Lip-Ce6-MnO_2 and Lip-Ce6-MnO_2-TPZ (n = 3); (d) absorbance spectrograms of Lip-Ce6-MnO_2 and Lip-Ce6-MnO_2-TPZ (10 μg mL^{-1}); (e) fluorescence emission spectra of Lip-Ce6-MnO_2 and Lip-Ce6-MnO_2-TPZ; (f) ratios of fluorescence intensity enhancement (F/F_0) of solutions containing Lip-Ce6-MnO_2 and Lip-Ce6-MnO_2-TPZ (10 μg mL^{-1}) (n = 3); (g) absorption spectra of MB solutions by Lip-Ce6-MnO_2 and Lip-Ce6-MnO_2-TPZ; and (h) HPLC verification of TPZ release from Lip-Ce6-MnO_2-TPZ.

528 nm was calculated (Fig. 2f and Fig. S2†). As we could see, the values gradually rose, verifying the efficient generation of $^1O_2$, which confirmed reliable sonodynamic effects in the following experiments. MB was used as a sensitive indicator of •OH radical production because it can degrade MB, reducing its absorbance intensity at its characteristic peak.[45] The absorbance peaks of Lip-Ce6-MnO_2 and Lip-Ce6-MnO_2-TPZ decreased under US, suggesting a more effective Fenton-like reaction, leading to greater •OH generation and faster MB degradation (Fig. 2g).[46] TPZ release under US stimuli was analyzed by HPLC (Fig. 2h). At 0 minutes, there was minimal detectable TPZ release, implying that TPZ was effectively encapsulated into the nanoparticles without ultrasound activation. The peak area for TPZ increased with time upon ultrasound activation (0, 5, 10, and 15 minutes), indicating that ultrasound facilitated the breakdown of the nanoparticle structure and a progressive release of TPZ.

3.2 Evaluation of SDT and CDT efficiency *in vitro*

Both Lip-Ce6-MnO_2 and Lip-Ce6-MnO_2-TPZ demonstrated good biocompatibility at concentrations up to 50 μg mL^{-1} in 4T1 cells (Fig. 3a). The cellular uptake of Lip-Ce6-MnO_2 and Lip-Ce6-MnO_2-TPZ was evaluated by flow cytometry, as we could see that the two nanoparticles had similar endocytosis efficiency as confirmed by quantitative analysis (Fig. 3b and c). The confocal microscopy image revealed that the nanoparticles were located in the cytosol after they were taken up. The quantitative analysis result of fluorescence from Ce6 was comparable, indicating that it had equal intracellular delivery efficiency (Fig. 3d and e), which was consistent with the flow cytometry results.

The ROS generation was evaluated by using the ROS probe. Without US irradiation, Lip-Ce6-MnO_2 and Lip-Ce6-MnO_2-TPZ exhibited minimal ROS generation as the image showed slight fluorescence comparable to that of PBS. This might be due to the small quantity of MnO_2 released from the nanoparticles into the cytosol and then reduced by GSH to Mn^{2+}, which triggered CDT for •OH production through a Fenton-like reaction. However, significantly higher green fluorescence was detected under US irradiation, suggesting that higher ROS levels and strong oxidative stress were induced by SDT and CDT subsequently (Fig. 4a and b). During SDT the MnO_2 in the nanoparticle would be reduced to Mn^{2+} by GSH in the cancer cells since it is abundant in the tumor environment and caused GSH depletion. We tested the GSH levels in 4T1 cells after nanoparticle treatment. Without US irradiation, the GSH level dropped slightly, which is possible because of the small amount of MnO_2 released from the nanoparticles as we had discussed above. Compared with groups that were not subjected to US stimuli, both Lip-Ce6-MnO_2 and Lip-Ce6-MnO_2-TPZ consumed GSH remarkably through redox reactions, demonstrating US induced disassembly of the nanoparticles, and facilitated the release of MnO_2 (Fig. 4c). Since hypoxia is a hallmark of many aggressive tumors and SDT might aggravate

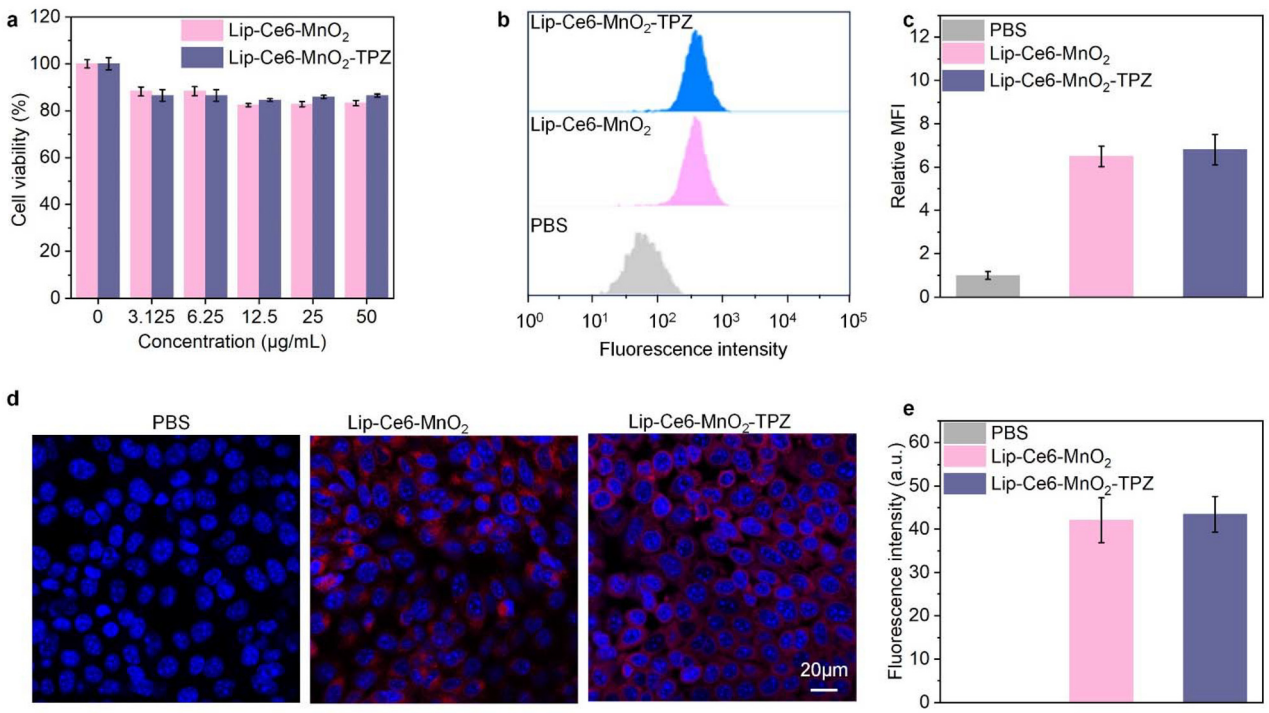

Fig. 3 Evaluation of *in vitro* therapeutic efficacy: (a) cell viability of 4T1 cells after incubation with Lip-Ce6-MnO_2 and Lip-Ce6-MnO_2-TPZ at different concentrations (n = 5); (b) fluorescence intensity analysis of Lip-Ce6-MnO_2 and Lip-Ce6-MnO_2-TPZ incubated 4T1 cells using flow cytometry; (c) quantitative analysis of cellular phagocytosis (n = 5); (d) representative confocal fluorescence images of Lip-Ce6-MnO_2 and Lip-Ce6-MnO_2-TPZ incubated 4T1 cells; and (e) quantitative analysis of confocal fluorescence (n = 5).

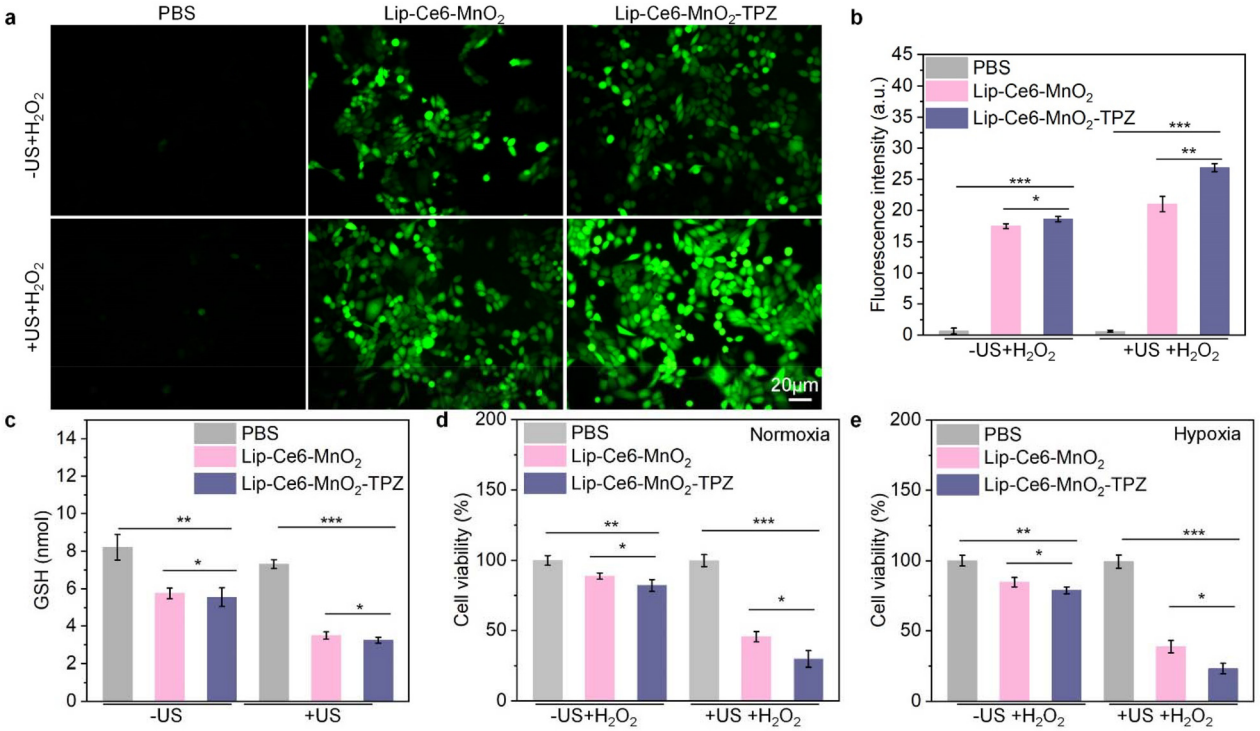

Fig. 4 ROS generation and functional characterization: (a) ROS fluorescence images of 4T1 cells in each group; (b) quantitative analysis of ROS fluorescence (n = 5); (c) levels of GSH in different treated 4T1 cells (n = 5); (d) cell viability of 4T1 cells under normoxic conditions (n = 5); (e) cell viability of 4T1 cells under hypoxic conditions (n = 5).

the hypoxic condition, we evaluated 4T1 cell viability under both normoxic and hypoxic conditions. As shown in Fig. 4d and e, SDT induced the decrease of cell viability to 45.5% and 29.7% for Lip-Ce6-MnO_2 and Lip-Ce6-MnO_2-TPZ, respectively, due to the cell killing effects of ROS. Under hypoxic conditions, TPZ demonstrated a selective cytotoxic effect by decreasing the cell viability to 38.7% and 23.1%, indicating that TPZ's efficacy could improve overall treatment outcomes by selectively killing the tumor cells. We also included experimental groups with single-component formulations (Lip-Ce6) and two-component formulations (Lip-Ce6-MnO_2 and Lip-Ce6-TPZ) to systematically evaluate their individual and combined effects. Our findings confirmed that Lip-Ce6-MnO_2-TPZ under US irradiation exhibited superior therapeutic efficacy compared to individual or dual-component formulations, supporting the hypothesis that the combination of all three components enhances therapeutic synergy (Fig. S3†).

3.3 Biodistribution and tumor retention efficiency

The biodistribution of Lip-Ce6-MnO_2 and Lip-Ce6-MnO_2-TPZ was evaluated in subcutaneous 4T1 tumor models. Both groups showed an accumulation of fluorescence signals at the tumor sites after intravenous injection (Fig. 5a) and an increase in signals over time was observed (Fig. 5b). The strongest fluorescence signal appeared around 24-hour post-injection, which might provide useful guidance for US stimulation in the following tumor therapy experiments. The fluorescence in other organs was also assessed at 24 h after injection (Fig. 5c) and both groups showed the highest signal at the tumor sites compared to other organs (Fig. 5d). These results indicated that the nanoparticles could efficiently accumulate at the tumor sites over time, holding great advantages in overcoming the physical barriers to penetrate tumors. The time-course analysis of biodistribution and *in vivo* clearance of nanoparticles was explored. The results showed a gradual decrease of fluorescence intensity in the livers, kidneys, and feces, almost absent by day 24 (Fig. S4 and S5†). After 24 days of administration, the fluorescence signal of the hearts, livers, spleens, lungs, and kidneys almost disappeared (Fig. S6†). These findings confirmed the safety profile of our nanoparticles. In addition, the pharmacokinetic properties of Lip-Ce6-MnO_2 and Lip-Ce6-MnO_2-TPZ were also explored. The nanoparticle concentration showed a gradual decrease in the bloodstream, until it approached a near-minimal level at 24 h, indicating that the nanoparticles were relatively cleared from circulation (Fig. S7†).

3.4 Evaluation of antitumor efficacy *in vivo*

Encouraged by the promising results from the above *in vitro* tumor cell inhibition and the accumulation ability at the tumor sites of Lip-Ce6-MnO_2 and Lip-Ce6-MnO_2-TPZ, we studied its therapeutic efficacy on subcutaneous 4T1 tumors in BALB/c mice. All animals showed steady mouse body weights indicating the great safety of the two nanoparticles (Fig. 6a).

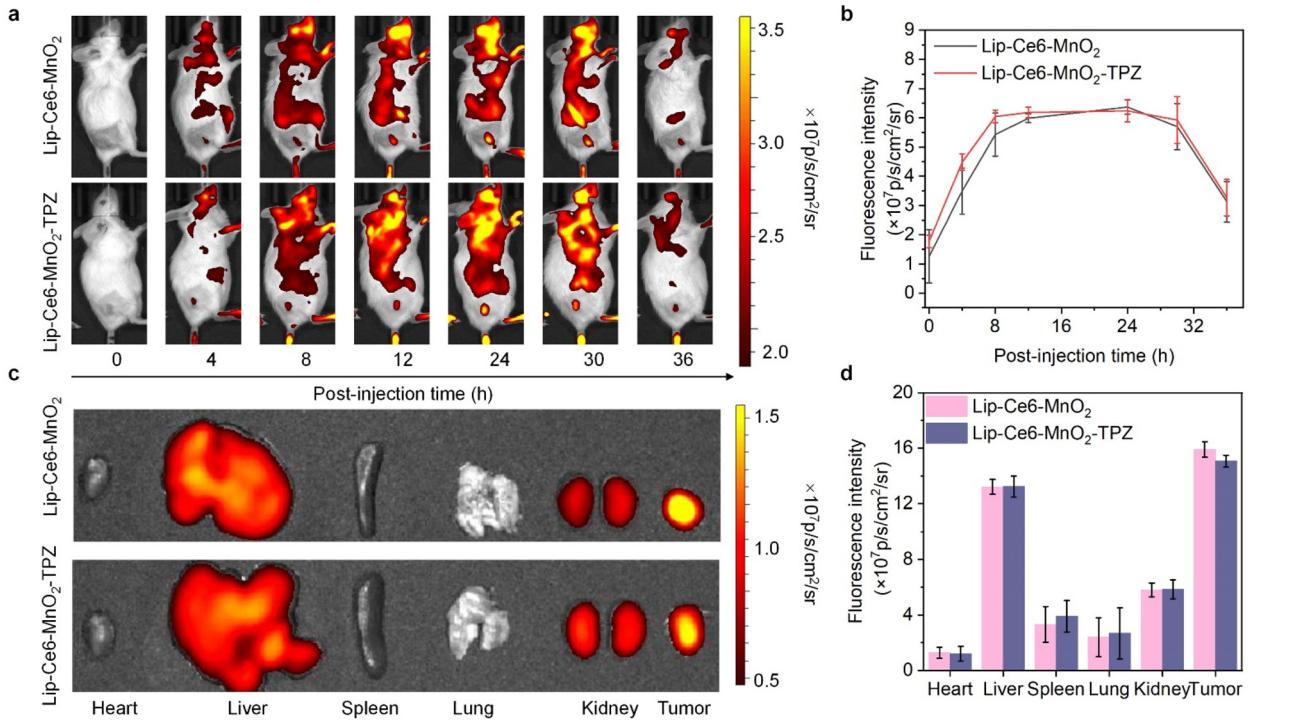

Fig. 5 *In vivo* fluorescence imaging: (a) fluorescence images of mice after injection of Lip-Ce6-MnO_2 and Lip-Ce6-MnO_2-TPZ through the tail vein at different time points; (b) intensity of fluorescence signals in the tumor areas of mice (n = 3); (c) fluorescence images of tumors and organs in mice 36 hours after intravenous injection of nanoparticles; and (d) quantitative analysis of fluorescence intensity in tumors and major organs (n = 3).

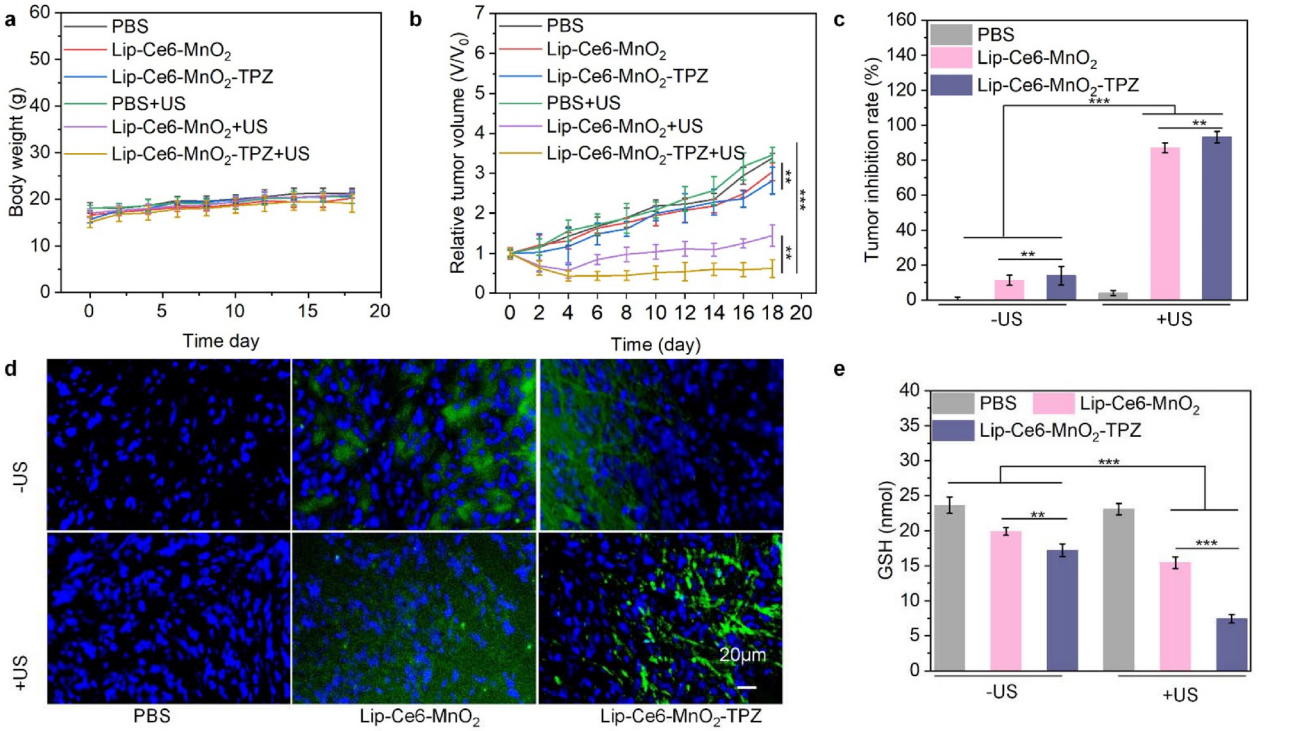

Fig. 6 *In vivo* therapeutic efficacy evaluation; (a) body weight in various groups after treatment (n = 5); (b) tumor volumes in various groups after treatment (n = 5); (c) the tumor inhibition efficacy in various treatment groups (n = 4); (d) images of ROS generation (green fluorescence signals) at tumor sites in various groups after treatments; (e) levels of GSH in tumors after treatment with PBS, Lip-Ce6-MnO_2 and Lip-Ce6-MnO_2-TPZ without or with US irradiation (n = 5).

Relative tumor volume was recorded twice a day until 18 days post-treatment (Fig. 6b). Both Lip-Ce6-MnO_2 and Lip-Ce6-MnO_2-TPZ with US stimuli showed significant efficacy in tumor suppression compared to other groups. Lip-Ce6-MnO_2-TPZ plus US irradiation exhibited the best therapeutic efficacy with a tumor inhibition of about 93.2% which was much higher than those of groups without US irradiation (Fig. 6c). At the end of the experiment, tumors from each group were collected, and the tumor photograph clearly showed the treatment efficiency of different groups (Fig. S8a†). The tumor weight was recorded, which showed consistent best tumor inhibition for Lip-Ce6-MnO_2-TPZ with US irradiation (Fig. S8b†).[47] After treatment, the mechanisms of SDT and CDT in the tumor sites were assessed. First, the ROS generation was evaluated by intraperitoneal injection of the ROS probe 24 h after nanoparticle injection. As could be seen from Fig. 6d, Lip-Ce6-MnO_2 and Lip-Ce6-MnO_2-TPZ under US stimulation showed diffused green fluorescence signals throughout the tumor section. The quantitative fluorescence intensity of the two groups was higher than those of the other groups (Fig. S9†), indicating the efficient generation of ROS during treatment. The GSH level at the tumor sites was also evaluated (Fig. 6e). Groups under US stimulation dramatically induced the reduction of GSH, indicating that the nanoparticle disassembly under US irradiation accelerated the release of MnO_2, and a robust reaction between MnO_2 and GSH caused the consumption of GSH. This result implied the antitumor efficiency of CDT.

As we all know, the 4T1 cell line is highly aggressive, which not only forms primary tumors but also exhibits spontaneous metastasis to distant organs, such as the lungs and liver, which are common secondary sites for 4T1.[48–50] After treatment, the lungs and liver were also collected for metastasis analysis by H&E staining. The staining images of the lungs showed visible metastatic tumor nodules for PBS, indicating significant tumor infiltration in the lung tissue. However, the number and size of metastatic nodules decreased, especially for Lip-Ce6-MnO_2-TPZ under US stimulation, demonstrating the treatment progress for this nanoparticle (Fig. 7a and b). Similar to the lung analysis, the liver H&E staining images of groups without US irradiation showed visible metastatic nodules disrupting normal liver architecture, indicating prominent tumor infiltration into the liver parenchyma (Fig. S10†). In contrast, treated groups under US stimulation demonstrated reduced tumor burden, especially Lip-Ce6-MnO_2-TPZ exhibited minimal metastatic nodules (Fig. 7c and d). This analysis highlighted the metastatic spread of cancer to both the lungs and liver, and Lip-Ce6-MnO_2-TPZ with US treatment was effective in reducing metastatic tumor burden in both the lungs and liver.

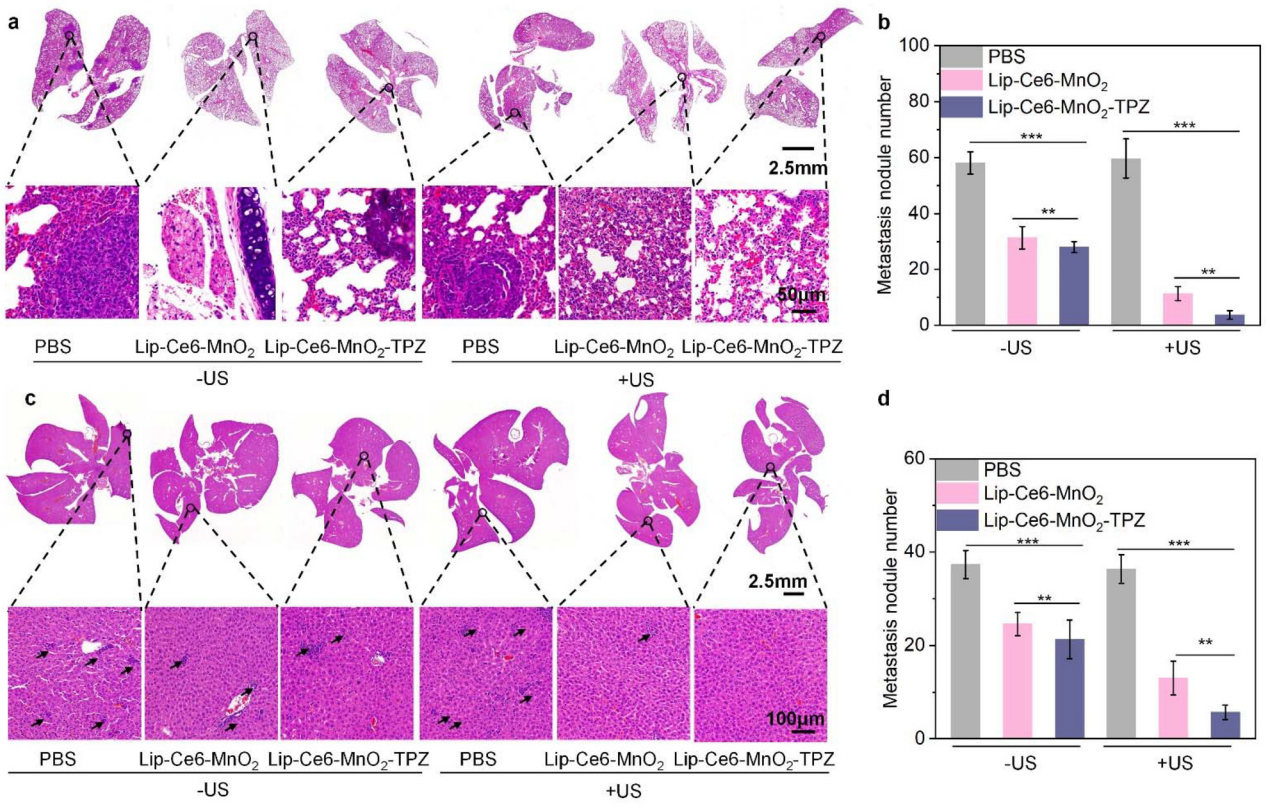

Fig. 7 *In vivo* antimetastatic efficacy evaluation; (a) analysis of lung metastasis inhibition in different treatment groups by H&E staining; (b) quantitative analysis of metastatic tumor nodules in the lungs (n = 3); (c) H&E staining was used to analyze the role of inhibition of liver metastasis in different treatment groups; and (d) quantitative analysis of metastatic tumor nodules in the liver (n = 3).

4. Conclusions

Unlike the normal tissues from which they originate, tumors are characterized by aberrant structures, impaired blood supply, and altered biochemical properties within their microenvironment. One of the most distinctive features of the TME is its hypoxic and acidic nature, often resulting from rapid tumor growth that outpaces the development of new blood vessels, creating regions of oxygen deprivation. These regions are typically more resistant to traditional therapies like radiation and chemotherapy, which rely on oxygen to generate cytotoxic effects. On the other hand, tumor cells exist in a delicate balance between the stress of ROS and antioxidant neutralization, which contributes to drug resistance and protects tumors from oxidative stress. Here, we developed a multifunctional nanoparticle Lip-Ce6-MnO_2-TPZ synergizing multiple therapeutic modalities, namely, ultrasound-triggered SDT, tumor microenvironment-targeted CDT, and hypoxia-specific drug into a single treatment platform. By combining these therapies, Lip-Ce6-MnO_2-TPZ could create a multifaceted attack on tumor cells, utilizing multiple therapeutic modalities to overcome treatment resistance and enhance the efficacy of cancer therapy. Specifically, we encapsulated the sonosensitizer Ce6, MnO_2, and hypoxia responsive drug tirapazamine (TPZ) together into a ROS responsive nanoparticle. Ce6 generated ROS under US stimuli could induce cancer cell apoptosis. Furthermore, ROS induced the acceleration of the nanoparticle disassembly to enhance the release of TPZ and MnO_2. As a result, SDT consumed oxygen and aggravated the hypoxic condition in the tumor site, leading to the activation of TPZ. Activated TPZ further enhances oxidative damage, leading to DNA damage and tumor cell death. Meanwhile, the MnO_2 was reduced to Mn^{2+} and caused GSH depletion. Subsequently, Mn^{2+} triggered CDT through a Fenton-like reaction by converting H_2O_2 to highly toxic •OH. The generation of excess ROS and antioxidant depletion combined together in the tumor cells caused aberrant redox homeostasis and modulation of the tumor microenvironment. The three-modality therapy showed significant advantages over single- or dual-modal treatment by leveraging multi-mechanistic synergy. When SDT or CDT was applied individually, the generation of ROS was limited and readily neutralized by glutathione (GSH) in the tumor microenvironments, particularly. For chemotherapy, it often resulted in high systemic toxicity and an increased likelihood of drug resistance. When using dual-mode treatment, such as SDT combined with CDT, although it enhanced oxidative damage, but would consume oxygen and further aggravate the hypoxic condition in the tumor site, limiting its overall therapeutic efficacy. In comparison, the combination of SDT, CDT and chemotherapy had significantly improved the anti-tumor effect and reduced the risk of side effects through multi-mechanism coordination, dose optimization and accurate delivery. Despite the technical complexity, its potential to overcome drug resistance and microenvironmental limitations provided a new direction for future tumor treatment. By targeting the tumor with multiple complementary mechanisms, these nanoparticles could significantly improve the effectiveness and specificity of cancer therapy, ultimately offering a more personalized and less invasive treatment option for patients. In conclusion, the use of a nanoplatform combining SDT, CDT, and hypoxia-specific drug represents a promising strategy for next-generation cancer treatments.

Author contributions

Chengxi Li, Can Yang and Tiantian Jiang share the first authorship. Jingchao Li, Yong Han and Ting Su share the corresponding authorship. Jingchao Li designed the project. Chengxi Li, Can Yang, Tiantian Jiang, Zheming Song and Danling Cheng performed the experiments. Yong Han and Ting Su interpreted and analyzed data. Chengxi Li, Can Yang, Tiantian Jiang and Ting Su wrote the paper.

Data availability

All data supporting the findings of this study are available in the paper and its ESI.†

Conflicts of interest

There are no conflicts to declare.

Acknowledgements

This work was supported by the Fundamental Research Funds for the Central Universities (2232024D-35) and Shanghai Songjiang District Science and Technology Research Project (2023SJKWGG044).

References

1 T. Suwa, M. Kobayashi, J. Nam and H. Harada, *Exp. Mol. Med.*, 2021, **53**, 1029–1035.
2 M. Li, Y. Liu, Y. Zhang, N. Yu and J. Li, *Adv. Sci.*, 2023, **10**, 2305150.
3 T. Hao, Y. Fu, Y. Yang, S. Yang, J. Liu, J. Tang, K. A. Ridwan, Y. Teng, Z. Liu, J. Li, N. Guo and P. Yu, *Eur. J. Med. Chem.*, 2021, **219**, 113430.
4 W. Chen, J. Liu, C. Zheng, Q. Bai, Q. Gao, Y. Zhang, K. Dong and T. Lu, *Int. J. Nanomed.*, 2022, **17**, 2611–2628.
5 Y. Zhuang, S. Han, Y. Fang, H. Huang and J. Wu, *Coord. Chem. Rev.*, 2022, **455**, 214360.
6 X. Jing, F. Yang, C. Shao, K. Wei, M. Xie, H. Shen and Y. Shu, *Mol. Cancer*, 2019, **18**, 157.
7 X. Zhang, X. Zhang, T. Yong, L. Gan and X. Yang, *eBioMedicine*, 2024, **105**, 105200.

8 K. F. Goliwas, J. S. Deshane, C. A. Elmets and M. Athar, *Physiol. Rev.*, 2021, **101**, 417–425.
9 H. Zhang, X. Zhang, Y. Ren, F. Cao, L. Hou and Z. Zhang, *Theranostics*, 2019, **9**, 3580–3594.
10 C. Cao, X. Wang, N. Yang, X. Song and X. Dong, *Chem. Sci.*, 2022, **13**, 863–889.
11 X. Qian, Y. Zheng and Y. Chen, *Adv. Mater.*, 2016, **28**, 8097–8129.
12 P. Wu, W. Dong, X. Guo, X. Qiao, S. Guo, L. Zhang, M. Wan and Y. Zong, *Adv. Healthcare Mater.*, 2019, **8**, 1900720.
13 J. Li and K. Pu, *Acc. Chem. Res.*, 2020, **53**, 752–762.
14 Y. Zhang, Y. Liu, Z. Li, Q. Zhang and J. Li, *Adv. Funct. Mater.*, 2025, **35**, 2412165.
15 Q. Li, B. Lin, Y. Li and N. Lu, *Int. J. Nanomed.*, 2021, **16**, 3875–3887.
16 Y. Zhang, Q. Zhang, F. Wang, M. Li, X. Shi and J. Li, *Nano Lett.*, 2023, **23**, 7699–7708.
17 C. Jia, Y. Guo and F. G. Wu, *Small*, 2021, **18**, 2103868.
18 L. Sun, X. Wang, F. Gong, K. Yin, W. Zhu, N. Yang, S. Bai, F. Liao, M. Shao and L. Cheng, *Theranostics*, 2021, **11**, 9234–9242.
19 X. Wang, X. Xu, Z. Yang, X. Xu, S. Han and H. Zhang, *Biomater. Sci.*, 2023, **11**, 7489–7511.
20 Y. Xin, Z. Guo, A. Ma, E. Shi, Z. Li, Z. Liang, Z. Qian, L. Yang, Y. Wang, M. Cao and X. Yang, *Chem. Eng. J.*, 2023, **451**, 138782.
21 X. Di, Z. Pei, Y. Pei and T. D. James, *Coord. Chem. Rev.*, 2023, **484**, 215098.
22 X. Huang, B. Feng, Y. Niu, L. Zhao and W. Hu, *Catal. Lett.*, 2018, **148**, 2528–2536.
23 Z. Tang, Y. Liu, M. He and W. Bu, *Angew. Chem., Int. Ed.*, 2018, **58**, 946–956.
24 J. Gu, D. Cheng, H. Li, T. Yu, Z. Zhang, Y. Liu, X. Wang, X. Lu and J. Li, *J. Mater. Chem. B*, 2024, **12**, 6091–6101.
25 Y. Liu, L. Wang, F. Wei, Y. Tian, J. Mou, S. Yang and H. Wu, *Biomater. Sci.*, 2023, **11**, 1739–1753.
26 H. He, L. Du, H. Xue, Y. An, K. Zeng, H. Huang, Y. He, C. Zhang, J. Wu and X. Shuai, *Small Methods*, 2023, **7**, 2300230.
27 H. Gao, Z. Cao, H. Liu, L. Chen, Y. Bai, Q. Wu, X. Yu, W. Wei and M. Wang, *Theranostics*, 2023, **13**, 1974–2014.
28 Z. Chen, Z. Li, C. Li, H. Huang, Y. Ren, Z. Li, Y. Hu and W. Guo, *Drug Delivery*, 2022, **29**, 1201–1211.
29 M. Ji, H. Liu, J. Gou, T. Yin, H. He, Y. Zhang and X. Tang, *Nanoscale*, 2023, **15**, 8948–8971.
30 Y. Deng, M. Ding, L. Zhu, Y. Zhang, F. Wang, L. Zhao and J. Li, *J. Mater. Chem. B*, 2023, **11**, 8484–8491.
31 Y. Wang, Q. Tang, R. Wu, S. Yang, Z. Geng, P. He, X. Li, Q. Chen and X. Liang, *ACS Nano*, 2024, **18**, 6314–6332.
32 P. Chang, Y. Guo, D. Chen, K. Li, W. Wang, Z. Yang, J. Ma, Y. Zeng, W. Zhan and Y. Zhan, *J. Nanobiotechnol.*, 2024, **22**, 374.
33 G. Canavese, A. Ancona, L. Racca, M. Canta, B. Dumontel, F. Barbaresco, T. Limongi and V. Cauda, *Chem. Eng. J.*, 2018, **340**, 155–172.
34 Y. Lee and D. H. Thompson, *Wiley Interdiscip. Rev.: Nanomed. Nanobiotechnol.*, 2017, **9**, e1450.
35 N. Yu, J. Zhou, H. Xu, F. Wang, X. Wang, L. Tang, J. Li, X. Wang and X. Lu, *Biomater. Adv.*, 2024, **163**, 213962.
36 Y. Hao, Y. Gao, Y. Fan, C. Zhang, M. Zhan, X. Cao, X. Shi and R. Guo, *J. Nanobiotechnol.*, 2022, **20**, 43.
37 Y. Tian, P. Li, L. Wang, X. Ye, Z. Qu, J. Mou, S. Yang and H. Wu, *Biomater. Sci.*, 2024, **12**, 2341–2355.
38 M. Wang, F. Li, T. Lu, R. Wu, S. Yang and W. Chen, *Mater. Des.*, 2022, **224**, 111403.
39 A. Zhu, W. Tu, M. Ding, Y. Zhang, J. Liu, X. Chen, L. Wang, Y. Liu and J. Li, *Chem. Eng. J.*, 2024, **497**, 154652.
40 H. Chen, Y. Fu, K. Feng, Y. Zhou, X. Wang, H. Huang, Y. Chen, W. Wang, Y. Xu, H. Tian, Y. Mao, J. Wang and Z. Zhang, *J. Nanobiotechnol.*, 2021, **19**, 298.
41 X. Guo, L. Han, W. Chen, H. He, W. Zhang, C. Huang and X. Wang, *Int. J. Nanomed.*, 2024, **19**, 247–261.
42 L. Liang, M. Jia, M. Zhao, Y. Deng, J. Tang, X. He, Y. Liu, K. Yan, X. Yu, H. Yang, C. Li, Y. Li and T. Li, *Int. J. Nanomed.*, 2024, **19**, 8883–8900.
43 Y. Liu and J. Wang, *Chem. Eng. J.*, 2023, **466**, 143147.
44 L. E. Franken, E. J. Boekema and M. C. A. Stuart, *Adv. Sci.*, 2017, **4**, 1600476.
45 Y. He, Z. Xu, Y. Yan, X. Zhang, Y. He, Q. Luo, D. Wang and D. Gao, *J. Colloid Interface Sci.*, 2024, **670**, 297–310.
46 Y. Nosaka and A. Nosaka, *ACS Energy Lett.*, 2016, **1**, 356–359.
47 C. Song, X. Wu, J. Wang, R. Liu and Y. Zhao, *Nano Today*, 2023, **51**, 101913.
48 X. Qiu, Z. Li, X. Han, L. Zhen, C. Luo, M. Liu, K. Yu and Y. Ren, *Theranostics*, 2019, **9**, 2618–2636.
49 H. Liu, X. Li, H. Li, L. Feng, G. Sun, G. Sun, L. Wu, Y. Hu, L. Liu and H. Wang, *Biomed. Pharmacother.*, 2022, **149**, 112824.
50 B. Medeiros and A. L. Allan, *Int. J. Mol. Sci.*, 2019, **20**, 2272.